ACS Catalysis

pubs.acs.org/acscatalysis

Research Article

Insulating High-Entropy Ruthenium Oxide as a Highly Efficient Oxygen-Evolving Electrocatalyst in Acid

Xianbing Miao, Zhen Peng,* Lei Shi, and Shiming Zhou*

Cite This: *ACS Catal.* 2023, 13, 3983−3989

Read Online

ACCESS | Metrics & More | Article Recommendations | Supporting Information

ABSTRACT: Designing efficient and economical oxygen-evolving catalysts in acid media is of prime importance to develop proton exchange membrane water electrolysis for hydrogen production but still remains a great challenge. Herein, by codoping of nonprecious Cr, W, and Cu elements into the lattice of RuIr-mixed oxide, we construct a high-entropy rutile $(Ru_{0.2}Ir_{0.2}Cr_{0.2}W_{0.2}Cu_{0.2})O_2$ as a superior catalyst for acidic water oxidation. This oxide exhibits a small overpotential of 220 mV at 10 mA cm^{-2}_{geo} with good stability in acidic electrolyte. Its mass activity reaches up to 1480.9 A $g^{-1}_{noble\ metal}$ at 1.53 V versus RHE, surpassing most reported Ru-based catalysts. Our microstructural analysis reveals that the multielement doping inhibits the crystalline grains coarsening due to the lattice distortion and hence increases the active surface areas. More interestingly, electronic structure studies demonstrate that these dopants result in a metal−insulator transition, which weakens the Ru−O binding strength and enhances the intrinsic activity of the active sites.

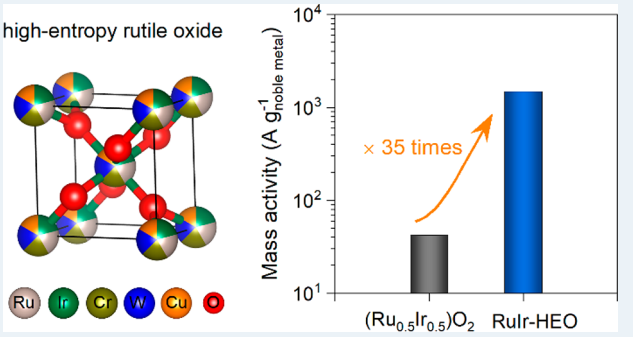

KEYWORDS: *oxygen evolution reaction, high-entropy compound, ruthenium oxide, lattice distortion, metal−insulator transition*

1. INTRODUCTION

The acidic proton exchange membrane (PEM) water electrolyzer serves as a promising technology for hydrogen production.[1,2] The efficiency of water splitting is significantly limited by the anodic oxygen evolution reaction (OER), which has a high overpotential due to the sluggish multistep proton-coupled electron transfer process.[3,4] Despite that these tremendous efforts have been devoted to exploring various OER catalysts, most of them still require considerably large overpotentials and cannot survive under the harsh acidic and oxidative environment.[4−6]

Up to now, precious-metal oxides of rutile RuO_2 and IrO_2 are the two most studied OER catalysts in acid.[5] The former exhibits a high OER activity but suffers from poor durability.[5,7,8] In contrast, the latter presents a high stability but relatively lower activity.[5,9] Accordingly, introducing Ir into the lattice of the former, for instance, to form $(Ru_{0.5}Ir_{0.5})O_2$, is widely regarded as a simple strategy to improve the acid resistance of Ru-based catalyst.[10−13] However, this strategy reduces the activity and increases the cost.[10,12] Therefore, developing highly active and durable acidic OER catalysts with low cost is still a great challenge.

High-entropy oxides (HEOs), defined as five or more near equimolar principal elements randomly distributed in a single-phase lattice, have attracted ever-increasing attention due to their unique physicochemical properties.[14−17] For precious-metal oxide catalysts, constructing high-entropy species with nonprecious metals greatly lowers the precious-metal usage. Meanwhile, multiple atoms occupying the equivalent lattice sites can generate lattice distortions and regulate the metal−oxygen covalencies.[16−18] Moreover, the configurational entropy from multielement mixing provides an additional contribution to the structure stability.[15,17] Inspired by such unique features, the high-entropy approach has been recently devoted to improving the OER activity of metal oxides.[19−21,23] For example, Yang et al.[20] reported that multielement codoping was conducive to inducing more high-valence Ni^{3+} species and thereby promoted the OER activity of high-entropy (HE) spinel $(Cr_{0.2}Mn_{0.2}Fe_{0.2}Ni_{0.2}Zn_{0.2})_3O_4$. Tang et al.[22] found that the incorporation of multiple atoms activated lattice oxygen sites by facilitating the formation of oxygen vacancies, endowing the HE perovskite $La_{0.6}Sr_{0.4}Co_{0.2}Fe_{0.2}Mn_{0.2}Ni_{0.2}Mg_{0.2}O_3$ with fast OER kinetics. Zhang et al.[23] demonstrated that a synergistic positive effect between incorporated elements improved the OER activity for the high-entropy Co−Cu−Fe−Mo (oxy)hydroxide. Despites these efforts, most of them involve the catalysts applied under alkaline conditions. Moreover, due to the complexity of HE materials, the underlying role of high-entropy induced

Received: December 20, 2022
Revised: February 13, 2023
Published: March 8, 2023

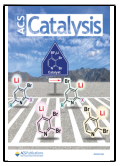

Downloaded from pubs.acs.org/acscatcs/article-pdf/13/6/3983/10248850/cs2c06276.pdf by DOKUZ EYLUL UNIV user on 30 August 2026

© 2023 American Chemical Society

https://doi.org/10.1021/acscatal.2c06276
ACS Catal. 2023, 13, 3983−3989

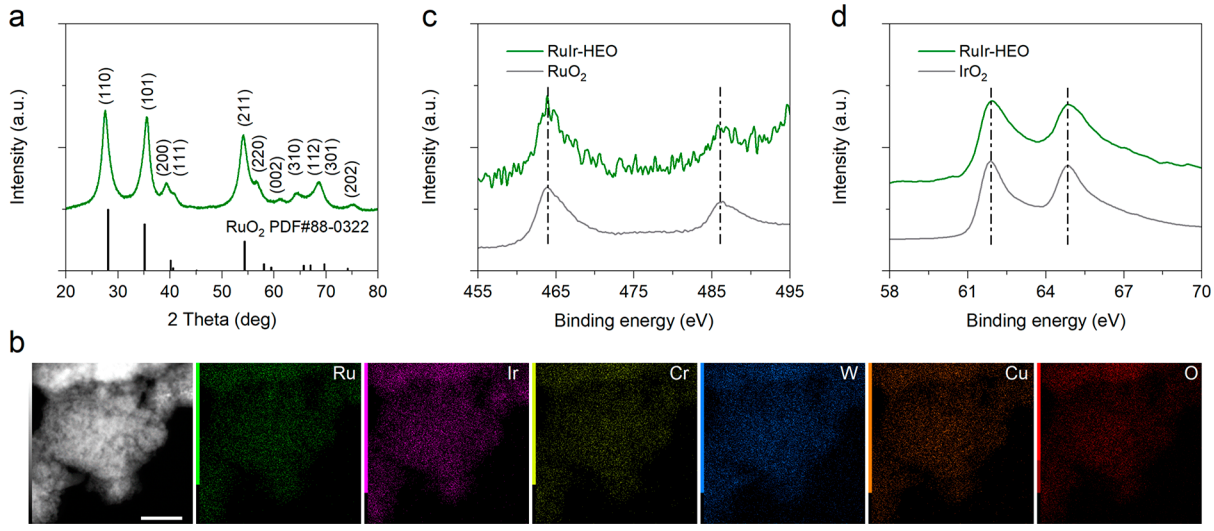

Figure 1. Structural characterization of RuIr-HEO. (a) XRD pattern. (b) EDS mapping. The scale bar is 50 nm. (c) Ru 3p and (d) Ir 4f XPS spectra of RuIr-HEO. Commercial RuO_2 and IrO_2 were used as the references.

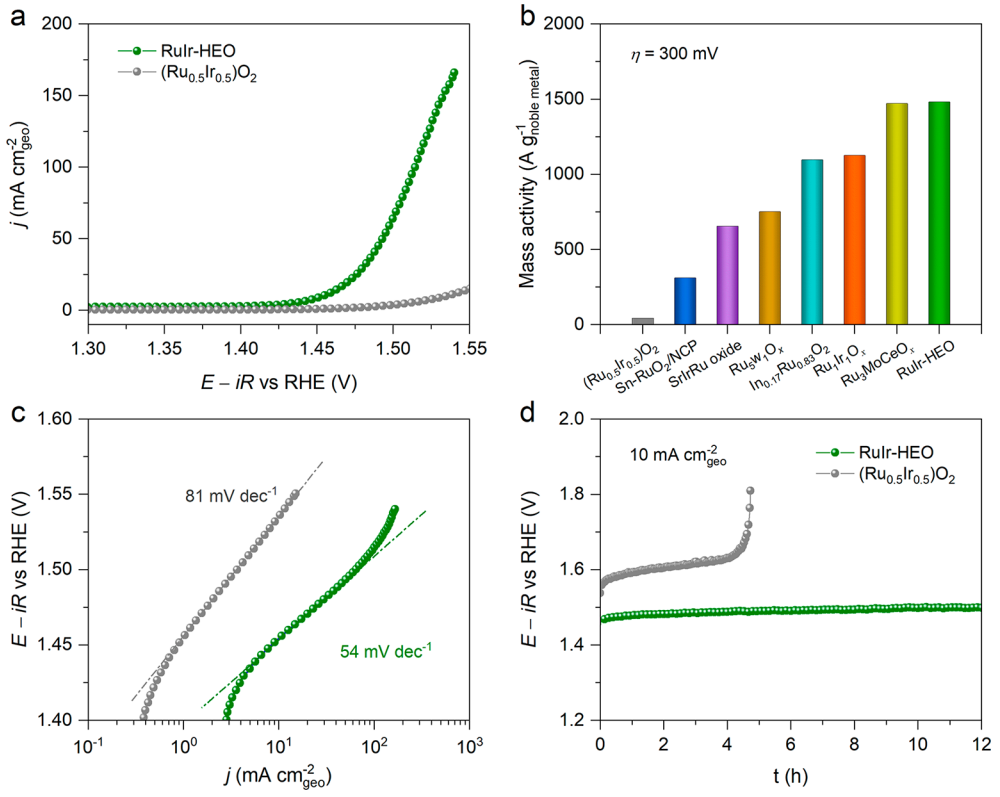

Figure 2. Electrochemical OER performance. (a) Polarization curves of RuIr-HEO and $(Ru_{0.5}Ir_{0.5})O_2$ catalysts recorded in O_2-saturated 0.5 M H_2SO_4 solution. (b) Comparison of mass activities at η = 300 mV for RuIr-HEO and recently reported Ru-based catalysts in acidic conditions. The references are listed in Table S1. (c) Tafel plots. (d) Chronopotentiometry tests at 10 mA cm^{-2}_{geo}.

microstructural and electronic structure features on the OER activity is elusive and remains unclear.

Herein, we successfully prepared high-entropy rutile oxide $(Ru_{0.2}Ir_{0.2}Cr_{0.2}W_{0.2}Cu_{0.2})O_2$ (RuIr-HEO) via codoping non-precious Cr, W, and Cu elements into $(Ru_{0.5}Ir_{0.5})O_2$ lattice. The as-prepared oxide effectively catalyzes water oxidation with a small overpotential of 220 mV and no significant deactivation after 12 h operation at 10 mA cm^{-2}_{geo} under pH = 0. More remarkably, the HEO catalyst presents a large mass activity of 1480.9 A $g^{-1}_{noble\ metal}$ at an overpotential of 300 mV, 35 times higher than that of binary $(Ru_{0.5}Ir_{0.5})O_2$. Our microstructural analysis demonstrates that the multielement doping induces a large lattice distortion, which refines the crystalline grains and increases the active surface areas. Furthermore, combining X-ray adsorption spectroscopy, X-ray photoelectron spectroscopy, and transport measurements, we find that introducing multiple-metal atoms into the lattice leads to a transition from a metal to insulator by diluting the RuO_6 octahedra connectivity, which weakens the Ru−O binding strength and hence enhances the intrinsic activity of

https://doi.org/10.1021/acscatal.2c06276
ACS Catal. 2023, 13, 3983−3989

Downloaded from pubs.acs.org/acscatcs/article-pdf/13/6/3983/10248850/cs2c06276.pdf by DOKUZ EYLUL UNIV user on 30 August 2026

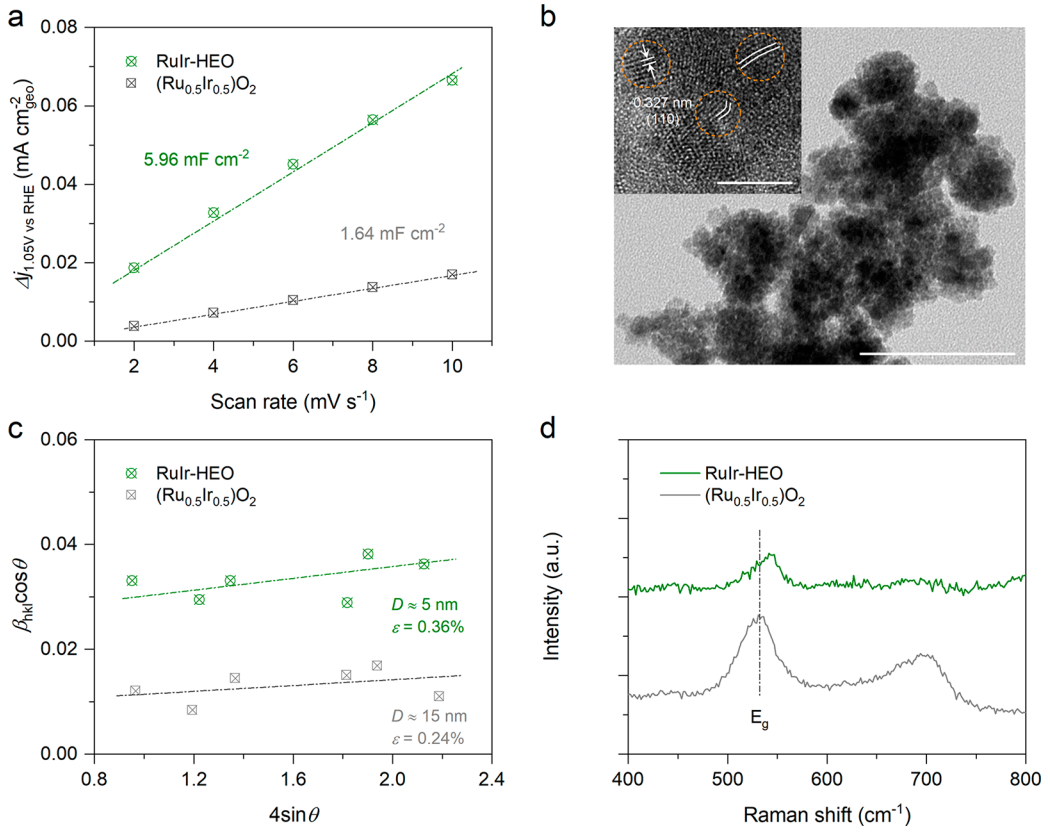

Figure 3. Microstructural analysis. (a) Plots of current density difference against scan rates and linear fitting for the evaluation of C_{dl} for RuIr-HEO and $(Ru_{0.5}Ir_{0.5})O_2$. $\Delta j_{1.05\ V\ vs\ RHE}$ is the difference between anodic and cathodic current densities at 1.05 V (vs RHE). (b) TEM image of RuIr-HEO with a scale bar of 100 nm. The inset shows the HRTEM image with a scale bar of 5 nm. The particles are marked by the orange circles. (c) The estimated grain size (D) and lattice strain (ε) from the Williamson−Hall analysis. (d) Raman spectra.

active sites. Both the increased number and reactivity of active sites facilitate the oxygen-evolving kinetics for the high-entropy catalyst.

2. RESULTS AND DISCUSSION

Polycrystalline powders of RuIr-HEO were prepared by a sol−gel method. The powder X-ray diffraction (XRD) pattern (Figure 1a) illustrates that as-prepared sample possesses a rutile-type structure, where all the diffraction peaks are indexed to the tetragonal phase with $P42/mnm$ space group. Scanning electron microscopy-energy dispersive X-ray spectroscopy (SEM-EDS, Figure S1) verifies the presence of Ru, Ir, Cr, W, and Cu elements with their atomic ratios of 1:0.97:0.97:1.03:1.14, which is very close to the nominal stoichiometry of 1:1:1:1:1. The EDS mapping analysis (Figure 1b) clearly reveals that all elements are uniformly distributed over the whole detection range, indicating the formation of high-entropy phase.

X-ray photoelectron spectroscopy (XPS) was performed to investigate the electronic states of RuIr-HEO. Figure 1c shows the Ru 3p core-level XPS spectra of the pentanary metal oxide, together with the commercial RuO_2 as a reference. Similar to those of RuO_2, two characteristic peaks around 464.2 and 486.3 eV were observed, which are assigned to $3p_{3/2}$ and $3p_{1/2}$ states of Ru^{4+} ions,[24] respectively. The Ir 4f XPS spectra (Figure 1d) display that the Ir $4f_{7/2}$ and $4f_{5/2}$ binding energies are located at 61.7 and 64.7 eV for RuIr-HEO, respectively, which are almost the same as those of commercial IrO_2 and indicative of Ir in the +4 valence state.[25,26] The Cr 2p spectrum shown in Figure S2a reveals that no obvious difference in the peak positions between RuIr-HEO and commercial CrO_2 can be found, suggesting that Cr ions are tetravalent. Figure S2b illustrates the W 4f XPS spectra of RuIr-HEO, where the peaks near 34.9 and 37.0 eV are attributed to W $4f_{7/2}$ and $4f_{5/2}$ states, respectively. Compared with those of commercial WO_3, the W 4f peaks for RuIr-HEO exhibit a noticeable negative shift and broadening, indicating that W ions are in a lower valence state than W^{6+}.[8,27] The Cu 2p XPS spectra of RuIr-HEO as plotted in Figure S2c present two deconvoluted peaks corresponding to low and high valence states of Cu ions,[28,29] respectively. The main peak around 933.7 eV is shifted toward higher binding energy region compared to that of commercial CuO, implying the existence of the Cu−O−M (M = Ru, Ir, Cr, or W) situation.[28,29]

The electrocatalytic OER performance of RuIr-HEO was evaluated in O_2-saturated 0.5 M H_2SO_4 electrolyte using a standard three-electrode setup. For comparison, binary $(Ru_{0.5}Ir_{0.5})O_2$, ternary $(Ru_{0.33}Ir_{0.33}Cr_{0.33})O_2$, and quaternary $(Ru_{0.25}Ir_{0.25}Cr_{0.25}W_{0.25})O_2$ were also synthesized and tested under the same conditions (Figure S3). The iR-corrected polarization curves for these RuIr-based catalysts, together with commercial RuO_2 as a reference, are shown in Figure 2a and Figure S4. The current density was found to increase with increasing the number of metal elements. To deliver a current density of 10 mA cm^{-2}_{geo}, RuIr-HEO just requires a small overpotential (η) of 220 mV, which is 85 and 64 mV lower than $(Ru_{0.5}Ir_{0.5})O_2$ and commercial RuO_2 (Figure S5a), respectively. The activity promotion in the high-entropy

https://doi.org/10.1021/acscatal.2c06276
ACS Catal. 2023, 13, 3983−3989

Downloaded from pubs.acs.org/acscatal/article-pdf/13/6/3983/10248850/cs2c06276.pdf by DOKUZ EYLUL UNIV user on 30 August 2026

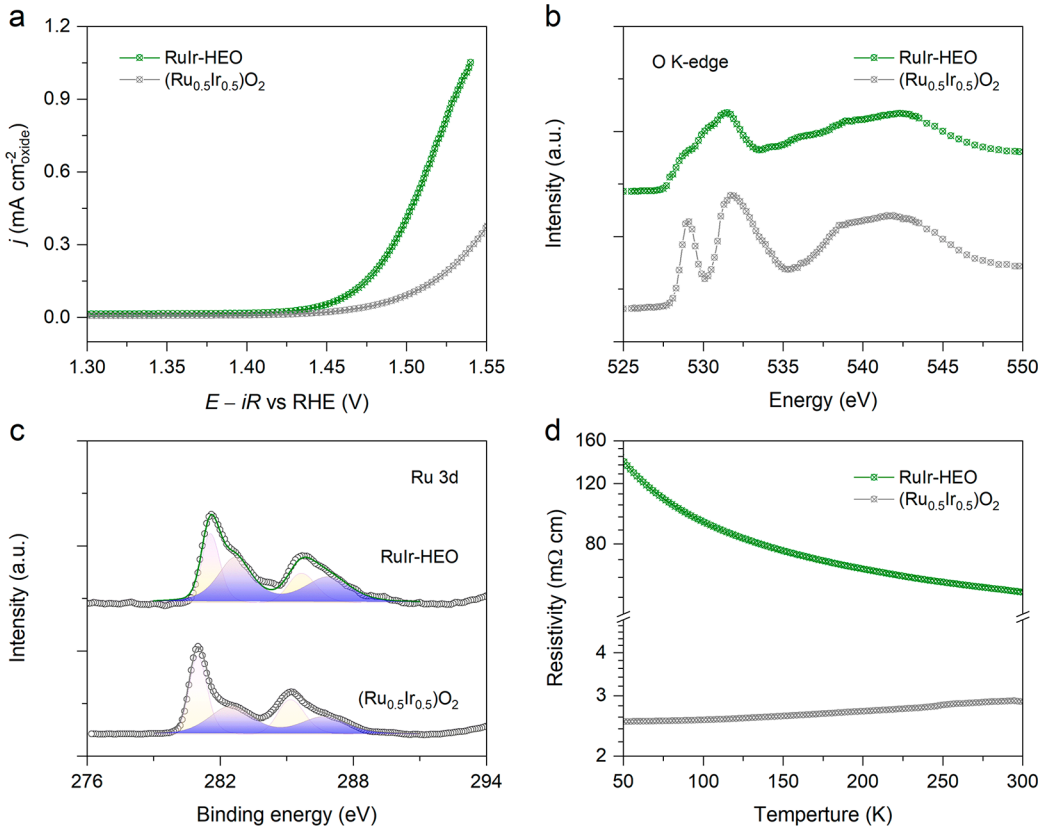

Figure 4. Intrinsic OER activity and electronic structure studies. (a) OER specific activity for RuIr-HEO and $(Ru_{0.5}Ir_{0.5})O_2$ oxides. (b) O K-edge XAS and (c) Ru 3d core-level XPS. In Ru 3d XPS, the doublets at lower and higher energies correspond to the screened (*s*) and unscreened (*u*) peaks, respectively. The dots are experimental data after the residual C 1s peaks are removed. (d) Temperature-dependent resistivity.

oxide was also reflected by the mass activity, obtained by normalizing the current density to the total loading mass of noble metal. Among these prepared catalysts, the pentanary oxide exhibits the highest mass activity of 1480.9 A $g^{-1}_{\text{noble metal}}$ at η = 300 mV, about 35 times larger than that of the binary oxide (42.3 A $g^{-1}_{\text{noble metal}}$) (Figure S5b). This value is also superior to those of recently reported Ru-based OER catalysts (Figure 2b and Table S1).

Figure 2c shows the Tafel plots derived from the polarization curves. Compared to $(Ru_{0.5}Ir_{0.5})O_2$ of 81 mV dec^{-1}, RuIr-HEO presents a smaller Tafel slope of 54 mV dec^{-1}, which suggests that the OER kinetics is accelerated in the high-entropy oxide. This result is further supported by the electrochemical impedance spectroscopy (EIS) measurements (Figure S6), where a smaller semicircle diameter for RuIr-HEO indicates its faster charge-transfer capability. Chronopotentiometric tests at a constant current density of 10 mA cm^{-2}_{geo} were carried out to assess the long-term stability of these catalysts. As displayed in Figure 2d, the catalytic stability of RuIr-HEO is far better than that of $(Ru_{0.5}Ir_{0.5})O_2$. The $(Ru_{0.5}Ir_{0.5})O_2$ catalyst nearly lost its activity within 5 h. However, RuIr-HEO remained stable with just a small increase in the potential of about 45 mV after a 12 h continuous operation. The high stability is also confirmed by the XRD and HRTEM measurements after the long-term operation. No noticeable change in the peak positions of XRD patterns (Figure S7) is found before and after OER testing. HRTEM images (Figure S8) show that lattice fringes of particles still extend all the way to the surface after the OER test, implying that its crystal structure is relatively stable during OER. These results demonstrate that the RuIr-HEO catalyst would be highly competitive in the potential commercial PEM water electrolysis.

To understand the enhanced OER activity in RuIr-HEO catalyst, we first assessed the electrochemically active surface areas (ECSA) via electrochemical double-layer capacitance (C_{dl}) measurements. As illustrated in Figure S9 and Figure 3a, RuIr-HEO presents a larger C_{dl} of 5.96 mF cm^{-2}, which is about 3.6 times higher than that of $(Ru_{0.5}Ir_{0.5})O_2$ (1.64 mF cm^{-2}). This means that the active surface area has a significant increase in the high-entropy catalyst. A similar result is also found in the Brunauer–Emmett–Teller (BET) surface area measurements (Figure S10), where RuIr-HEO exhibits a much larger BET surface area of 63.18 m^2 g^{-1} than $(Ru_{0.5}Ir_{0.5})O_2$ (15.99 m^2 g^{-1}). An increase in the active surface areas is ascribed to a remarkable reduction in the average particle size from about ∼20 to ∼5 nm upon codoping, as supported by transmission electron microscopy (TEM) images (Figure S11 and Figure 3b). In high-entropy materials, it has been reported that grain coarsening can be inhibited due to the lattice distortion arising from the size mismatch of different metal ions occupying the same lattice sites.[14,16] To further investigate the microstructural features in these samples, we analyzed the widths of their XRD peaks, which are related to the grain size and lattice distortion.[30] We found that RuIr-HEO displays significantly broadening diffraction peaks in comparison to $(Ru_{0.5}Ir_{0.5})O_2$ (Figure S12). According to the Williamson–Hall analysis,[31] the grain size and lattice strain are estimated to be ∼15 nm and ∼0.24% for $(Ru_{0.5}Ir_{0.5})O_2$, respectively. However, for RuIr-HEO, the former decreases to ∼5 nm and the latter

https://doi.org/10.1021/acscatal.2c06276
ACS Catal. 2023, 13, 3983−3989

Downloaded from pubs.acs.org/acscacs/article-pdf/13/6/3983/10248850/cs2c06276.pdf by DOKUZ EYLUL UNIV user on 30 August 2026

increases to ~0.36% (Figure 3c). The substantial reduction in the grain size is well consistent with the TEM results, which suggests the existence of grain refining in the high-entropy sample. Moreover, we further conducted Raman spectra to study the local structure, as shown in Figure 3d. Compared to $(Ru_{0.5}Ir_{0.5})O_2$, the characteristic peak around 530 cm^{-1} assigned to E_{1g} vibration mode of the rutile structure exhibits a noticeable blue-shift and asymmetric broadening in RuIr-HEO, verifying the increase in the lattice distortion.[32,33] The presence of large lattice distortion in the high-entropy sample is further confirmed by HRTEM images. As displayed in Figure S13a, the regular atomic arrangements in crystal lattice are observed for $(Ru_{0.5}Ir_{0.5})O_2$, where the identified lattice spacing of 0.319 nm corresponds to the (110) plane from the rutile. However, for RuIr-HEO, the HRTEM images (the inset of Figure 3b and Figure S13b-d) show that the lattice spacing for (110) plane exhibits an obvious increase to 0.327 nm upon codoping, which is in line with the downshift of (110) diffraction peak in the XRD patterns (Figure S12). More interestingly, the atomic arrangements in the lattice are found to be significantly distorted, which gives direct evidence of large lattice distortion in this sample. These results reveal that the increased surface areas originating from lattice strain-induced grain refining provide more active sites and thus boost the OER for HEO-RuIr.

Next, we further evaluated the intrinsic OER activity by normalizing the current density with the BET surface areas for our catalysts. As displayed in Figure 4a, the obtained specific activity still exhibits a remarkable promotion in HEO-RuIr. For example, at η = 300 mV, the specific activity of HEO-RuIr reaches up to 0.91 mA cm^{-2}_{oxide}, which is about 4.1 times higher than that of $(Ru_{0.5}Ir_{0.5})O_2$ (0.22 mA cm^{-2}_{oxide}). This means that the high-entropy strategy not only increases the number of active sites but also enhances the reactivity of active sites. The conventional adsorbate mechanism demonstrates that the intrinsic OER activity is determined by the binding strengths of oxygenated intermediates to active sites.[34,35] For rutile RuO_2, its large OER overpotential is widely believed to derive from the strong binding between the oxygen intermediates and Ru sites.[8,29,36] Our recent work has reported that weakening the Ru−O bonding strength by downshifting the Ru 4d-band center could effectively lower the overpotential.[37] To characterize the strength of the Ru−O bond in our catalysts, we carried out O K-edge X-ray adsorption spectroscopy (XAS) measurements. As shown in Figure 4b, two pre-edge peaks appear around 535 eV, which are assignable to the transitions from O 1s core level to unoccupied O 2p states hybridized with metal d-orbitals.[38,39] The normalized intensity of these peaks reflects the hybridization strength of metal−oxygen bonds, where a smaller intensity suggests a weaker hybridization. Obviously, the normalized intensity for RuIr-HEO is much smaller than that of $(Ru_{0.5}Ir_{0.5})O_2$, which suggests that the Ru−O bonds in the high-entropy oxide have a much less hybridization and hence a weaker strength.

In rutile RuO_2, the RuO_6 octahedra are connected in a mixture of corner and edge-sharing networks. The high degree of RuO_6 connectivity and the large spatial extension of Ru 4d-orbitals lead to a wide Ru 4d-band, which crosses the Fermi level and results in a metallic behavior.[40,41] When the heteroions are introduced to the lattice, the RuO_6 connectivity, i.e., the Ru−O−Ru network, is diluted. Consequently, the Ru 4d-band would be narrowed and pushed away from the Fermi level.[42−44] To explore the doping effect on the electronic structure of the rutile catalyst, we performed the Ru 3d core-level XPS measurements. As shown in Figure 4c, two sharp peaks are well resolved at 281.0 and 285.2 eV for both the oxides, which are designated as the emissions from Ru $3d_{3/2}$ and $3d_{5/2}$ core levels, respectively. Besides the sharp main peaks, two broad shoulder peaks can be also detected at higher energies. The sharp and broad peaks correspond to the screened (s) and unscreened (u) states.[42,43] Generally, the s peaks reflect the coherent metallic states around the Fermi level.[43] Compared with $(Ru_{0.5}Ir_{0.5})O_2$, RuIr-HEO presents a much decrease in the relative intensity between s and u peaks from 1.13 to 0.71, which indicates that the conduction electron density significantly decreases.[42,43] In other words, the density of states around the Fermi level would be reduced by Cr, W, and Cu codoping. This feature is further supported by the temperature-dependent resistivity measurements (Figure 4d). For $(Ru_{0.5}Ir_{0.5})O_2$, the resistivity decreases upon cooling, signifying its metallic behavior. By contrast, the resistivity of RuIr-HEO shows a monotonous increase as the temperature decreases, reflecting its insulating nature. Moreover, the resistivity of the latter is apparently higher than that of the former within the measured temperature range. For instance, RuIr-HEO exhibits a 20-fold increase in the resistivity (57.9 mΩ cm) at room temperature compared to $(Ru_{0.5}Ir_{0.5})O_2$ of 2.9 mΩ cm. The observed metal−insulator transition confirms that the Cr, W, and Cu codoping pushes the density of states away from the Fermi level and downshifts the Ru 4d-band center. The lowered Ru 4d-band center results in the weakened Ru−O binding strength.[45,46] Therefore, for RuIr-HEO, the binding energy between adsorbed oxygen species and Ru sites is reduced and then its intrinsic OER activity is enhanced. Of note, the high conductivity is widely considered to be beneficial for the OER process because it ensures fast charge transfer between the catalysts and electrolyte.[47,48] Our finding that the insulating RuIr-HEO outperforms the metallic $(Ru_{0.5}Ir_{0.5})O_2$ is quite surprising, which demonstrates that more suitable adsorption energies between oxygen intermediates and Ru active sites in RuIr-HEO play a key role in its accelerated OER kinetics.

3. CONCLUSION

In summary, we develop a high-entropy rutile oxide $(Ru_{0.2}Ir_{0.2}Cr_{0.2}W_{0.2}Cu_{0.2})O_2$ as a highly efficient catalyst toward acidic OER. We find that multielement doping inhibits the grain coarsening due to the lattice distortion, resulting in a large surface area for the pentanary metal oxide. Moreover, the electronic structure studies reveal that these dopants dilute the RuO_6 octahedra connectivity in the rutile lattice and make the high-entropy oxide insulating, which is accompanied by a weakening of Ru−O binding strength and an optimized adsorption of oxygen intermediates. Both the above features endow the as-prepared high-entropy catalyst with fast OER kinetics. Our work not only offers deep insight into the high-entropy effect on the activity of OER catalysts but also points toward a direction to design highly efficient oxide catalysts applied in acidic PEM water electrolyzer.

■ ASSOCIATED CONTENT

Supporting Information

The Supporting Information is available free of charge at https://pubs.acs.org/doi/10.1021/acscatal.2c06276.

Downloaded from pubs.acs.org/acscatcs/article-pdf/13/6/3983/10248850/cs2c06276.pdf by DOKUZ EYLUL UNIV user on 30 August 2026

https://doi.org/10.1021/acscatal.2c06276
ACS Catal. 2023, 13, 3983−3989

Experimental procedures, characterization data (including XRD, XPS spectra, HRTEM images, etc.), and electrochemical data (PDF)

AUTHOR INFORMATION

Corresponding Authors

Zhen Peng − *School of Materials Science and Engineering, Jiangsu University, Zhenjiang, Jiangsu 212013, P. R. China*; Email: peng@ujs.edu.cn

Shiming Zhou − *Hefei National Research Center for Physics Sciences at the Microscale, University of Science and Technology of China, Hefei, Anhui 230026, P. R. China*; orcid.org/0000-0002-1597-6060; Email: zhousm@ustc.edu.cn

Authors

Xianbing Miao − *Hefei National Research Center for Physics Sciences at the Microscale, University of Science and Technology of China, Hefei, Anhui 230026, P. R. China*

Lei Shi − *Hefei National Research Center for Physics Sciences at the Microscale, University of Science and Technology of China, Hefei, Anhui 230026, P. R. China*; orcid.org/0000-0002-0947-6617

Complete contact information is available at: https://pubs.acs.org/10.1021/acscatal.2c06276

Notes

The authors declare no competing financial interest.

ACKNOWLEDGMENTS

This work was financially supported by the National Science Foundation of China (grant nos. 92163106, 21972132, and 52271147) and China Postdoctoral Science Foundation (2021M703065).

REFERENCES

(1) Carmo, M.; Fritz, D. L.; Mergel, J.; Stolten, D. A comprehensive review on PEM water electrolysis. *Int. J. Hydrogen Energy* **2013**, *38*, 4901−4934.

(2) Kibsgaard, J.; Chorkendorff, I. Considerations for the scaling-up of water splitting catalysts. *Nat. Energy.* **2019**, *4*, 430−433.

(3) Seitz, L. C.; Dickens, C. F.; Nishio, K.; Hikita, Y.; Montoya, J.; Doyle, A.; Kirk, C.; Vojvodic, A.; Hwang, H. Y.; Norskov, J. K.; Jaramillo, T. F. A highly active and stable $IrO_x/SrIrO_3$ catalyst for the oxygen evolution reaction. *Science* **2016**, *353*, 1011−1014.

(4) Blasco-Ahicart, M.; Soriano-López, J.; Carbó, J. J.; Poblet, J. M.; Galan-Mascaros, J. R. Polyoxometalate electrocatalysts based on earth-abundant metals for efficient water oxidation in acidic media. *Nat. Chem.* **2018**, *10*, 24−30.

(5) Lee, Y.; Suntivich, J.; May, K. J.; Perry, E. E.; Shao-Horn, Y. Synthesis and activities of rutile IrO_2 and RuO_2 nanoparticles for oxygen evolution in acid and alkaline solutions. *J. Phys. Chem. Lett.* **2012**, *3*, 399−404.

(6) McCrory, C. C.; Jung, S.; Ferrer, I. M.; Chatman, S. M.; Peters, J. C.; Jaramillo, T. F. Benchmarking hydrogen evolving reaction and oxygen evolving reaction electrocatalysts for solar water splitting devices. *J. Am. Chem. Soc.* **2015**, *137*, 4347−4357.

(7) Roy, C.; Rao, R. R.; Stoerzinger, K. A.; Hwang, J.; Rossmeisl, J.; Chorkendorff, I.; Shao-Horn, Y.; Stephens, I. E. L. Trends in activity and dissolution on RuO_2 under oxygen evolution conditions: particles versus well-defined extended surfaces. *ACS Energy Lett.* **2018**, *3*, 2045−2051.

(8) Hao, S.; Liu, M.; Pan, J.; Liu, X.; Tan, X.; Xu, N.; He, Y.; Lei, L.; Zhang, X. Dopants fixation of ruthenium for boosting acidic oxygen evolution stability and activity. *Nat. Commun.* **2020**, *11*, 5368.

(9) Geiger, S.; Kasian, O.; Ledendecker, M.; Pizzutilo, E.; Mingers, A. M.; Fu, W. T.; Diaz-Morales, O.; Li, Z.; Oellers, T.; Fruchter, L.; Ludwig, A.; Mayrhofer, K. J. J.; Koper, M. T. M.; Cherevko, S. The stability number as a metric for electrocatalyst stability benchmarking. *Nat. Catal.* **2018**, *1*, 508−515.

(10) Kötz, R.; Stucki, S. Stabilization of RuO_2 by IrO_2 for anodic oxygen evolution in acid media. *Electrochim. Acta* **1986**, *31*, 1311−1316.

(11) Danilovic, N.; Subbaraman, R.; Chang, K. C.; Chang, S. H.; Kang, Y.; Snyder, J.; Paulikas, A. P.; Strmcnik, D.; Kim, Y. T.; Myers, D.; Stamenkovic, V. R.; Markovic, N. M. Using surface segregation to design stable Ru-Ir oxides for the oxygen evolution reaction in acidic environments. *Angew. Chem., Int. Ed.* **2014**, *53*, 14016−14021.

(12) Kasian, O.; Geiger, S.; Stock, P.; Polymeros, G.; Breitbach, B.; Savan, A.; Ludwig, A.; Cherevko, S.; Mayrhofer, K. J. J. On the origin of the improved ruthenium stability in RuO_2-IrO_2 mixed oxides. *J. Electrochem. Soc.* **2016**, *163*, F3099−F3104.

(13) Nguyen, T. D.; Nguyen, H. H.; Dai, C.; Wang, J.; Scherer, G. G. Activity and stability optimization of $Ru_xIr_{1-x}O_2$ nanocatalyst for the oxygen evolution reaction by tuning the synthetic process. *Int. J. Hydrogen Energy* **2020**, *45*, 46−55.

(14) Oses, C.; Toher, C.; Curtarolo, S. High-entropy ceramics. *Nat. Rev. Mater.* **2020**, *5*, 295−309.

(15) Li, T.; Yao, Y.; Huang, Z.; Xie, P.; Liu, Z.; Yang, M.; Gao, J.; Zeng, K.; Brozena, A. H.; Pastel, G.; Jiao, M.; Dong, Q.; Dai, J.; Li, S.; Zong, H.; Chi, M.; Luo, J.; Mo, Y.; Wang, G.; Wang, C.; Shahbazian-Yassar, R.; Hu, L. Denary oxide nanoparticles as highly stable catalysts for methane combustion. *Nat. Catal.* **2021**, *4*, 62−70.

(16) Yang, B.; Zhang, Y.; Pan, H.; Si, W.; Zhang, Q.; Shen, Z.; Yu, Y.; Lan, S.; Meng, F.; Liu, Y.; Huang, H.; He, J.; Gu, L.; Zhang, S.; Chen, L.-Q.; Zhu, J.; Nan, C.-W.; Lin, Y.-H. High-entropy enhanced capacitive energy storage. *Nat. Mater.* **2022**, *21*, 1074−1080.

(17) Zhang, R.; Wang, C.; Zou, P.; Lin, R.; Ma, L.; Yin, L.; Li, T.; Xu, W.; Jia, H.; Li, Q.; Sainio, S.; Kisslinger, K.; Trask, S. E.; Ehrlich, S. N.; Yang, Y.; Kiss, A. M.; Ge, M.; Polzin, B. J.; Lee, S. J.; Xu, W.; Ren, Y.; Xin, H. L. Compositionally complex doping for zero-strain zero-cobalt layered cathodes. *Nature* **2022**, *610*, 67−73.

(18) Su, L.; Huyan, H.; Sarkar, A.; Gao, W.; Yan, X.; Addiego, C.; Kruk, R.; Hahn, H.; Pan, X. Direct observation of elemental fluctuation and oxygen octahedral distortion-dependent charge distribution in high entropy oxides. *Nat. Commun.* **2022**, *13*, 2358.

(19) Zhang, Y.; Lu, T.; Ye, Y.; Dai, W.; Zhu, Y.; Pan, Y. Stabilizing oxygen vacancy in entropy-engineered $CoFe_2O_4$-type catalysts for Co-prosperity of efficiency and stability in an oxygen evolution reaction. *ACS Appl. Mater. Interfaces* **2020**, *12*, 32548−32555.

(20) Yang, X.; Liping, S.; Qiang, L.; Lihua, H.; Hui, Z. Co-prosperity of electrocatalytic activity and stability in high entropy spinel $(Cr_{0.2}Mn_{0.2}Fe_{0.2}Ni_{0.2}Zn_{0.2})_3O_4$ for the oxygen evolution reaction. *J. Mater. Chem. A* **2022**, *10*, 17633−17641.

(21) Wu, H.; Lu, Q.; Li, Y.; Wang, J.; Li, Y.; Jiang, R.; Zhang, J.; Zheng, X.; Han, X.; Zhao, N.; Li, J.; Deng, Y.; Hu, W. Rapid Joule-heating synthesis for manufacturing high-entropy oxides as efficient electrocatalysts. *Nano Lett.* **2022**, *22*, 6492−6500.

(22) Tang, L.; Yang, Y.; Guo, H.; Wang, Y.; Wang, M.; Liu, Z.; Yang, G.; Fu, X.; Luo, Y.; Jiang, C.; Zhao, Y.; Shao, Z.; Sun, Y. High configuration entropy activated lattice oxygen for O_2 formation on perovskite electrocatalyst. *Adv. Funct. Mater.* **2022**, *32*, 2112157.

(23) Zhang, L.; Cai, W.; Bao, N.; Yang, H. Implanting an electron donor to enlarge the d-p hybridization of high-entropy (oxy)-hydroxide: a novel design to boost oxygen evolution. *Adv. Mater.* **2022**, *34*, 2110511.

(24) Li, G.; Li, S.; Ge, J.; Liu, C.; Xing, W. Discontinuously covered IrO_2-RuO_2@Ru electrocatalysts for the oxygen evolution reaction: how high activity and long-term durability can be simultaneously realized in the synergistic and hybrid nano-structure. *J. Mater. Chem. A* **2017**, *5*, 17221−17229.

(25) Gao, J.; Xu, C.-Q.; Hung, S.-F.; Liu, W.; Cai, W.; Zeng, Z.; Jia, C.; Chen, H. M.; Xiao, H.; Li, J.; Huang, Y.; Liu, B. Breaking long-

Downloaded from pubs.acs.org/acscacs/article-pdf/13/6/3983/10248850/cs2c06276.pdf by DOKUZ EYLUL UNIV user on 30 August 2026

range order in iridium oxide by alkali ion for efficient water oxidation. *J. Am. Chem. Soc.* **2019**, *141*, 3014−3023.
(26) Yin, J.; Jin, J.; Lu, M.; Huang, B.; Zhang, H.; Peng, Y.; Xi, P.; Yan, C.-H. Iridium single atoms coupling with oxygen vacancies boosts oxygen evolution reaction in acid media. *J. Am. Chem. Soc.* **2020**, *142*, 18378−18386.
(27) Zheng, T.; Sang, W.; He, Z.; Wei, Q.; Chen, B.; Li, H.; Cao, C.; Huang, R.; Yan, X.; Pan, B.; Zhou, S.; Zeng, J. Conductive tungsten oxide nanosheets for highly efficient hydrogen evolution. *Nano Lett.* **2017**, *17*, 7968−7973.
(28) Sun, W.; Song, Y.; Gong, X.-Q.; Cao, L.-M.; Yang, J. An efficiently tuned d-orbital occupation of IrO_2 by doping with Cu for enhancing the oxygen evolution reaction activity. *Chem. Sci.* **2015**, *6*, 4993−4999.
(29) Yang, K.; Xu, P.; Lin, Z.; Yang, Y.; Jiang, P.; Wang, C.; Liu, S.; Gong, S.; Hu, L.; Chen, Q. Ultrasmall Ru/Cu-doped RuO_2 complex embedded in amorphous carbon skeleton as highly active bifunctional electrocatalysts for overall water splitting. *Small* **2018**, *14*, 1803009.
(30) Jiang, B.; Yu, Y.; Cui, J.; Liu, X.; Xie, L.; Liao, J.; Zhang, Q.; Huang, Y.; Ning, S.; Jia, B.; Zhu, B.; Bai, S.; Chen, L.; Pennycook, S. J.; He, J. High-entropy-stabilized chalcogenides with high thermoelectric performance. *Science* **2021**, *371*, 830−834.
(31) Williamson, G. K.; Hall, W. H. X-ray line broadening from filed aluminium and wolfram. *Acta Metall.* **1953**, *1*, 22−31.
(32) Huang, Y. S.; Pollak, F. H. Raman investigation of rutile RuO_2. *Solid State Commun.* **1982**, *43*, 921−924.
(33) Rosenblum, S. S.; Weber, W. H.; Chamberland, B. L. Raman-scattering observation of the rutile-to-$CaCl_2$ phase transition in RuO_2. *Phys. Rev. B* **1997**, *56*, 529−533.
(34) Man, I. C.; Su, H.-Y.; Calle-Vallejo, F.; Hansen, H. A.; Martinez, J. I.; Inoglu, N. G.; Kitchin, J.; Jaramillo, T. F.; Nørskov, J. K.; Rossmeisl, J. Universality in oxygen evolution electrocatalysis on oxide surfaces. *ChemCatChem.* **2011**, *3*, 1159−1165.
(35) Montoya, J. H.; Doyle, A. D.; Nørskov, J. K.; Vojvodic, A. Trends in adsorption of electrocatalytic water splitting intermediates on cubic ABO_3 oxides. *Phys. Chem. Chem. Phys.* **2018**, *20*, 3813−3818.
(36) Xu, Z.; Rossmeisl, J.; Kitchin, J. R. A linear response DFT + U study of trends in the oxygen evolution activity of transition metal rutile dioxides. *J. Phys. Chem. C* **2015**, *119*, 4827−4833.
(37) Miao, X.; Zhang, L.; Wu, L.; Hu, Z.; Shi, L.; Zhou, S. Quadruple perovskite ruthenate as a highly efficient catalyst for acidic water oxidation. *Nat. Commun.* **2019**, *10*, 3809.
(38) Grimaud, A.; May, K. J.; Carlton, C. E.; Lee, Y.-L.; Risch, M.; Hong, W. T.; Zhou, J.; Shao-Horn, Y. Double perovskites as a family of highly active catalysts for oxygen evolution in alkaline solution. *Nat. Commun.* **2013**, *4*, 2439.
(39) Suntivich, J.; Hong, W. T.; Lee, Y.-L.; Rondinelli, J. M.; Yang, W.; Goodenough, J. B.; Dabrowski, B.; Freeland, J. W.; Shao-Horn, Y. Estimating hybridization of transition metal and oxygen states in perovskites from O K-edge X-ray absorption spectroscopy. *J. Phys. Chem. C* **2014**, *118*, 1856−1863.
(40) Imada, M.; Fujimori, A.; Tokura, Y. Metal-insulator transitions. *Rev. Mod. Phys.* **1998**, *70*, 1039−1263.
(41) Ryden, W. D.; Lawson, A. W.; Sartain, C. C. Electrical transport properties of IrO_2 and RuO_2. *Phys. Rev. B* **1970**, *1*, 1494.
(42) Kawasaki, J. K.; Uchida, M.; Paik, H.; Schlom, D. G.; Shen, K. M. Evolution of electronic correlations across the rutile, perovskite, and Ruddelsden-Popper iridates with octahedral connectivity. *Phys. Rev. B* **2016**, *94*, 121104.
(43) Tsuda, S.; Kikugawa, N.; Sugii, K.; Uji, S.; Ueda, S.; Nishio, M.; Maeno, Y. Mott transition extremely sensitive to impurities in $Ca_3Ru_2O_7$ revealed by hard x-ray photoemission studies. *Phys. Rev. B* **2013**, *87*, 241107.
(44) Huon, A.; Yoon, S.; Fitzsimmons, M. R.; Charlton, T. R.; Ok, J. M.; Cruz, C. D.; Lee, H. N. Effects of Sn substitution in $SrRuO_3$ epitaxial films. *Appl. Phys. Lett.* **2021**, *119*, 112404.
(45) Dickens, C. F.; Montoya, J. H.; Kulkarni, A. R.; Bajdich, M.; Nørskov, J. K. An electronic structure descriptor for oxygen reactivity at metal and metal-oxide surfaces. *Surf. Sci.* **2019**, *681*, 122−129.
(46) Ling, C.; Shi, L.; Ouyang, Y.; Zeng, X. C.; Wang, J. Nanosheet supported single-metal atom bifunctional catalyst for overall water splitting. *Nano Lett.* **2017**, *17*, 5133−5139.
(47) Xu, K.; Chen, P.; Li, X.; Tong, Y.; Ding, H.; Wu, X.; Chu, W.; Peng, Z.; Wu, C.; Xie, Y. Metallic nickel nitride nanosheets realizing enhanced electrochemical water oxidation. *J. Am. Chem. Soc.* **2015**, *137*, 4119−4125.
(48) Zhao, X.; Zhang, H.; Yan, Y.; Cao, J.; Li, X.; Zhou, S.; Peng, Z.; Zeng, J. Engineering the electrical conductivity of lamellar silver-doped cobalt(II) selenide nanobelts for enhanced oxygen evolution. *Angew. Chem., Int. Ed.* **2017**, *56*, 328−332.

Downloaded from pubs.acs.org/acscacs/article-pdf/13/6/3983/10248850/cs2c06276.pdf by DOKUZ EYLUL UNIV user on 30 August 2026

https://doi.org/10.1021/acscatal.2c06276
ACS Catal. 2023, 13, 3983−3989